International Journal of Heat and Mass Transfer 51 (2008) 6283–6293

Contents lists available at ScienceDirect

International Journal of Heat and Mass Transfer

journal homepage: www.elsevier.com/locate/ijhmt

Experimental and numerical study of convection heat transfer of CO_2 at supercritical pressures in vertical porous tubes

Pei-Xue Jiang *, Run-Fu Shi, Chen-Ru Zhao, Yi-Jun Xu

Key Laboratory for Thermal Science and Power Engineering of Ministry of Education, Department of Thermal Engineering, Tsinghua University, Beijing 100084, China

ARTICLE INFO

Article history:
Received 21 October 2006
Received in revised form 15 May 2008
Available online 9 July 2008

Keywords:
Convection heat transfer
Flow resistance
Porous media
Supercritical carbon dioxide
Experimental investigation
Numerical simulation

ABSTRACT

Convection heat transfer of CO_2 at supercritical pressures in vertical sintered porous tubes with particle diameters of 0.1–0.12 mm and 0.2–0.28 mm was investigated experimentally and numerically. The study investigated the influence of the inlet fluid temperature, mass flow rate, pressure, particle diameter, heat flux, flow direction and buoyancy on convection heat transfer in porous tubes. The results show that the inlet temperature, pressure, mass flow rate, particle diameter and heat flux all strongly influence the convection heat transfer at supercritical pressures. When the inlet temperature is much larger than the pseudocritical temperature, T_{pc}, the local heat transfer coefficients in porous tubes are much less than when the inlet temperature is less than T_{pc}. For $T_0 < T_{pc}$ and wall temperatures not much larger than T_{pc}, the local heat transfer coefficients have a maximum for both upward flow and downward flow along the porous tube when the fluid bulk temperatures are near T_{pc}. Buoyancy caused the different variations in the local heat transfer coefficients along the porous tube for upward and downward flows. The results also show that the heat transfer coefficients increase as the particle diameter decrease. The numerical simulations were performed using the local thermal equilibrium model with consideration of the effects of variable porosity, thermal dispersion and area-of-contact stagnant effective thermal conductivity. The experimental and numerical results for the friction factor of CO_2 at supercritical pressures flowing in sintered porous tubes at constant temperature (without heating) corresponded very well with the known correlation. However, the predicted results for the friction factor of CO_2 at supercritical pressures flowing in the heated sintered porous tube differ from those measured in the experiments both for upward and downward flows. The calculated wall temperatures corresponded well with the measured wall temperatures.

1. Introduction

Supercritical pressure fluids have been used with porous media in many areas, such as for extraction and separation processes in chemical engineering, transpiration cooling in rocket thruster chambers, transpiring wall in supercritical water oxidation systems, and underground CO_2 storage. However, the mechanisms of fluid flow and convection heat transfer of supercritical pressure fluids in porous media are not yet well understood. Investigations of convection heat transfer in fluids at supercritical pressures in porous media will facilitate help development of these systems. Transpiration cooling is one of the most efficient methods to protect high temperature surfaces such as rocket thrusters with a gas such as hydrogen at supercritical pressures used as the coolant flowing through a porous wall. In supercritical water oxidation systems, supercritical pressure water is used as the oxidant flowing through a porous wall to prevent salt deposits and to reduce corrosion.

Convection heat transfer of supercritical pressure fluids has many special features due to the sharp variations of the thermophysical properties, especially the variation of c_p. Buoyancy caused by the density variations significantly affects the convection heat transfer of supercritical pressure fluids. There has been extensive research on internal forced and mixed convection heat transfer of supercritical fluids in normal size tubes in the past 50 years by Petukhov [1], Hall [2], Jackson [3], Krasnoshchekov and Protopopov [4], Protopopov [5], Popov and Valueva [6], Kurganov and Kaptilnyi [7], Jiang et al. [8], and He et al. [9]. Recently, with decreasing channel sizes, research on the convection heat transfer of supercritical pressure fluids has focused on mini/micro scale tubes such as by Liao and Zhao [10], Jiang et al. [11] and He et al. [12]. However, to the authors' knowledge, there is very limited work on convection heat transfer of supercritical fluids in porous media [11,13,14]. The convection heat transfer of normal fluids such as water and air in porous media has been investigated for relatively small variations of the fluid thermophysical properties with

* Corresponding author. Tel.: +86 10 62772661.
E-mail address: jiangpx@mail.tsinghua.edu.cn (P.-X. Jiang).

0017-9310/$ - see front matter © 2008 Elsevier Ltd. All rights reserved.
doi:10.1016/j.ijheatmasstransfer.2008.05.014

Nomenclature

c_p	specific heat at constant pressure (J/(kg K))
d	tube inner diameter (m)
d_p	particle diameter (m)
G	mass flow rate (kg/s)
Gr	Grashof number, $Gr = gd_p^3\rho(\rho_b - \rho_w)/\mu^2$
$h_{f,0}$	inlet specific enthalpy (J/kg)
$h_{f,b}(x)$	local fluid bulk enthalpy (J/kg)
h_x	local heat transfer coefficient (W/(m^2 K))
K	thermal conductivity (W/(mK))
M	mass flux (=ρu) (kg/(m^2 s))
P	pressure (Pa)
q_w	heat flux on the inner tube surface (W/m^2)
Re	Reynolds number, $Re = \rho u d_p/\mu$
Re_e	equivalent Reynolds number
T	temperature (° C) or (K)
T_{pc}	pseudocritical temperature (° C) or (K)
u	x-direction velocity component (m/s)
x	axial coordinate (m)

Greek symbols

ρ	density (kg/m^3)
μ	dynamic viscosity (kg/(m s))
δ	distance from thermocouples to the inner surface (m)
ε	porosity

Subscripts

b	bulk
dis	dispersion
d_p	particle diameter
d_w	downward flow
f	fluid
i	inner surface
s	solid wall
u_p	upward flow
w	wall
δ	outer mini-channels of the tube which hold the thermocouples
0	tube inlet

temperature and pressure theoretically, numerically and experimentally by Vafai and Tien [15], Cheng and Hsu [16], Hunt and Tien [17], Hsu and Cheng [18], Amiri et al. [19], Jeigarnik et al. [20], Achenbach [21], Lage et al. [22], Quintard [23], Jiang et al. [24,25,27], and Alazmi and Vafai [26].

Jiang et al. [11,14] presented experimental results for convection heat transfer of CO_2 at supercritical pressures in a vertical porous tube with particle diameters of 0.2–0.28 mm. Two new correlations were presented for upward and downward flows to predict the friction factors of supercritical pressure CO_2 in heated porous tubes. The results show that the inlet temperature, pressure and heat flux all strongly influence the convection heat transfer at supercritical pressures. However, in these previous studies [11,14] the fluid flow and convection heat transfer of CO_2 at supercritical pressures in only one porous tube with particle diameter of 0.2–0.28 mm was investigated experimentally, and there was no attempt to numerically simulate the process.

This paper reports new experimental results for the convection heat transfer of CO_2 at supercritical pressures in a vertical porous tube for upward and downward flows with particle diameters of 0.1–0.12 mm and 0.2–0.28 mm, and compares the convection heat transfer effects in the two tubes with different particle diameters. In addition, the convection heat transfer of CO_2 at supercritical pressures in vertical porous tubes is studied numerically using the local thermal equilibrium model.

2. Experimental system and data reduction

Fig. 1 shows the experimental system, which included a compressed CO_2 container, a cooling water bath and chiller, a high pressure CO_2 pump and a high pressure magnetic pump, a Coriolis mass flow meter, a pre-heater, an accumulator to eliminate the mass flow rate fluctuations, a test section, an after cooler, pressure gauges, pressure and differential pressure transducers, electrical power input and measurement systems, and a data acquisition system (HP 34970A).

The test sections shown in Fig. 2 were porous cylindrical tubes with inside and outside diameters of 4 mm and 6 mm containing particles with diameters of 0.1–0.12 mm and 0.2–0.28 mm. The heated length of the test sections was 50 mm. The porous tubes were made from a pure copper tube filled with sintered bronze particles. The porosity in the porous tube with particles having diameters of 0.1–0.12 mm was about 0.45, while the porosity in the porous tube with particles having diameters of 0.2–0.28 mm was about 0.4. The test section was heated using electrical resistance wire wrapped around and electrically isolated from the tube. CO_2 flowed into the test section from the bottom for upward flow and from the top for downward flow.

The parameters measured in the experiments included the wall temperatures, the mass flow rate, the inlet and outlet temperatures, the inlet pressure, the pressure drop across the test section, the electrical resistance, and the heater voltages. The local tube wall temperature was measured with 8 copper-constantan thermocouples inserted into mini-channels cut into the test section surface (0.2 mm deep by 0.2 mm wide) along the tube. Mixers were installed before and after the test section to mix the fluid before the inlet and outlet fluid temperatures were measured by accurate platinum thermal resistance thermometers (RTD). The inlet pressure was measured using a pressure transducer (Model

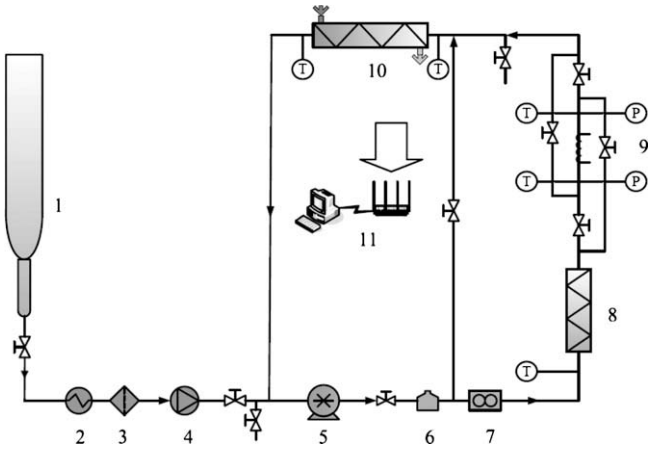

Fig. 1. Experimental system. 1. CO_2 container; 2. cooling water bath; 3. filter; 4. supercritical CO_2 pump; 5. pump; 6. accumulator; 7. flowmeter; 8. pre-heater; 9. test section; 10. cooler; 11. data acquisition system.

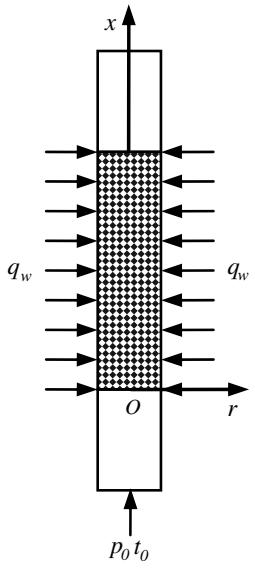

Fig. 2. Test section schematic.

EJA430A) with a full range of 12 MPa. The test section pressure drop was measured using a differential pressure transducer (Model EJA110A) with a full range of 500 kPa. The mass flow rate was measured using a Coriolis-type mass flowmeter (Model MASS2100/MASS6000, MASSFLO, Danfoss) with a full range of 65 kg/h.

Steady state was reached in the experiments after a long time (e.g. 50–120 min). The system was determined to be at steady state when the variations of the wall temperatures and the inlet and outlet fluid temperatures were all within ±0.1 °C and the variations of the flow rate and the inlet pressure were all within ±0.2% for at least 10 min.

The local temperatures of the inner surface of the porous circular tube were calculated using the measured outer surface temperatures of the tube, $T_{w,\delta}(x)$, assuming one-dimensional steady heat conduction in the wall:

$$T_{w,i}(x) = T_{w,\delta}(x) - \frac{q_w d}{2k_s} \ln\frac{d+2\delta}{d} \quad (1)$$

where δ indicates the tube wall thickness.

The local heat transfer coefficient, h_x, at each axial location was calculated as

$$h_x = \frac{q_w}{T_{w,i}(x) - T_{f,b}(x)} \quad (2)$$

The local bulk fluid temperature, $T_{f,b}(x)$, was calculated from the local bulk fluid enthalpy, $h_{f,b}(x)$, using

$$h_{f,b}(x) = h_{f,0} + \frac{q_w \pi d x}{G} \quad (3)$$

The Reynolds number based on the mean fluid temperature and the particle diameter was defined as

$$Re_{d_p} = \frac{\rho u d_p}{\mu} = \frac{4G d_p}{\pi d^2 \mu} \quad (4)$$

Prior to installation, the thermocouples and the RTDs were calibrated by the National Institute of Metrology, PR China. The accuracies were within ±0.1 °C in the temperature range of 0–70 °C and ±0.2 °C in the temperature range of 70–150 °C. The accuracy of the pressure transducer was 0.075% of the full range of 12 MPa. The accuracy of the differential pressure transducer was 0.075% of the full range of 500 kPa. According to the instructions, the accuracy of the Coriolis-type mass flowmeter was 0.1% of the actual mass flow rate with 95% confidence for flow rates of 5–100% of the sensor's maximum flow rate. For flow rates less than 5% of the sensor's maximum flow rate, the following formula should be used to calculate the error:

$$\varepsilon_G = \pm\sqrt{0.1^2 + \left(\frac{Z\times 100}{m}\right)^2}$$

where ε_G = error (%), Z = zero point error (kg/h) (=0.002 kg/h), and m = mass flow (kg/h). The minimum flow rate during the measurements was 0.5 kg/h. Therefore, the maximum relative uncertainty of the mass flow rate was ±0.4%.

The experimental uncertainty of the wall heat flux was mainly due to the heat loss which had a maximum of ±6.6% in present experimental cases. Thus, the uncertainty of the wall heat flux was about ±6.61%. The uncertainty of the difference between the wall temperature and the fluid temperature was about 6.25%, and the uncertainty of the heating area measured by vernier calipers with a precision of 0.002 mm was 0.3%; therefore, according to the definition of the convection heat transfer coefficients, Eq. (2), the maximum experimental uncertainty of the convection heat transfer coefficient was estimated to be ±13.2%. The experimental uncertainty in the inlet pressures was estimated to be ±0.13% and the maximum uncertainty of the pressure drop was estimated to be ±3.8%.

3. Experimental results and discussion

Fig. 3 shows the thermophysical properties of CO_2 at 8.5 and 9.5 MPa calculated using NIST REFPROP 7.1 [28]. The pseudocritical

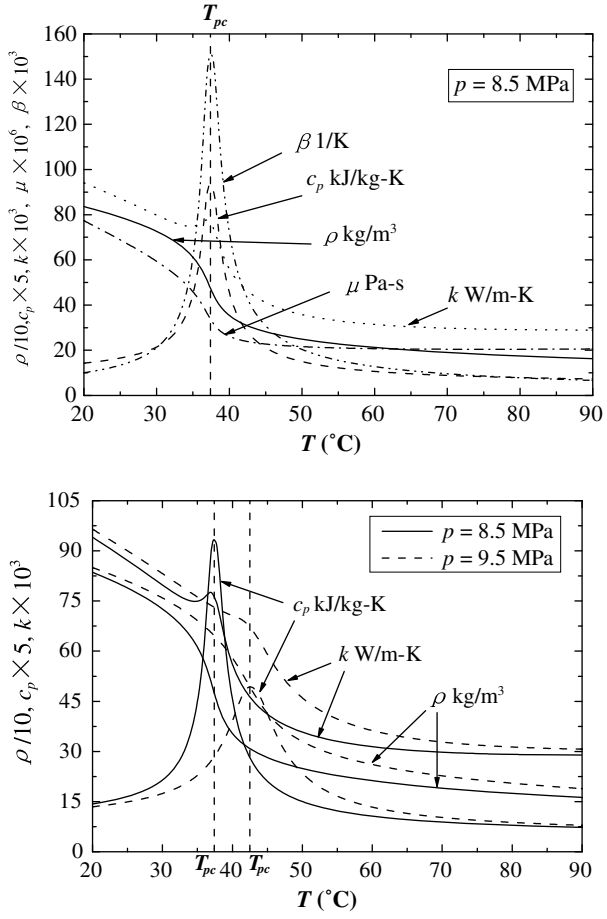

Fig. 3. Thermophysical properties of CO_2.

temperatures, T_{pc}, are 37.4 °C and 42.5 °C for CO_2 at these pressures. The thermophysical properties of CO_2 at supercritical pressures sharply vary with fluid temperature and pressure with the specific heat having a maximum at the pseudocritical temperature.

Figs. 4–11 present the experimental results for the local heat transfer coefficients and the wall and fluid bulk temperatures for convection heat transfer of CO_2 at supercritical pressures in the sintered vertical porous tubes with particle diameters of 0.2–0.28 mm and 0.1–0.12 mm for upward and downward flows. The experimental results for the porous tube with particle diameters of 0.1–0.12 mm are compared with results for the porous tube with particle diameters of 0.2–0.28 mm in Figs. 12 and 13. In these figures, the solid symbols are the data for upward flow, while the hollow symbols are the data for downward flow. The fluid bulk temperatures were calculated from the local pressure and the local enthalpy.

3.1. Influence of inlet temperatures

Figs. 4 and 5 show the wall and fluid bulk temperature distributions and the local heat transfer coefficients for various inlet temperatures. For the same pressure, mass flow rate and heat flux, the convection heat transfer coefficients are vary significantly for different inlet temperatures due to the strong variations of the thermophysical properties of supercritical CO_2 with temperature for both upward and downward flows.

There are three different cases for the wall and fluid temperature relationships, $T_f < T_w < T_{pc}$ (Fig. 5 with $T_{f,0} = 30$ °C), $T_f < T_{pc} < T_w$ (Fig. 4 with $T_{f,0} = 30$ °C, Figs. 4 and 5 with $T_{f,0} = 40$ °C), and $T_{pc} < T_f < T_w$ (Figs. 4 and 5 with $T_{f,0} = 45$ °C) where $T_{pc} = 42.5$ °C for CO_2 at 9.5 MPa. The local heat transfer coefficients for the second case with $T_f < T_{pc} < T_w$ are larger than for the other two cases due to the large value of c_p in this range as shown in Fig. 3. For $T_f < T_w < T_{pc}$, the local heat transfer coefficients increase along the porous tube due to increase in c_p. When the inlet temperature is higher than the pseudocritical temperature with $T_{pc} < T_f < T_w$ (such as $T_{f,0} = 45$ °C at 9.5 MPa), the local heat transfer coefficients decrease continuously along the porous tube due to decrease of the thermophysical properties along the porous tube, especially the decreases in c_p. However, when the inlet temperature is less than T_{pc} and the wall temperature is larger than T_{pc}, the local heat transfer coefficients experience complex variations along the porous tube. This phenomenon can be easily understood from Fig. 3, which shows that c_p varies sharply with temperature with a maximum at T_{pc}.

3.2. Influence of heat flux

Figs. 6 and 7 illustrate the influence of heat flux on the wall and fluid bulk temperatures and on the local heat transfer coefficients along the porous tube for $T_0 < T_{pc}$. The influence of the heat flux on the local heat transfer coefficients is complicated for $T_0 < T_{pc}$ depending on the local wall and local fluid temperature relationships, as shown in Section 3.1. The local heat transfer coefficients first increase with increasing heat flux to a maximum at a moderate heat flux and then decrease with increasing heat

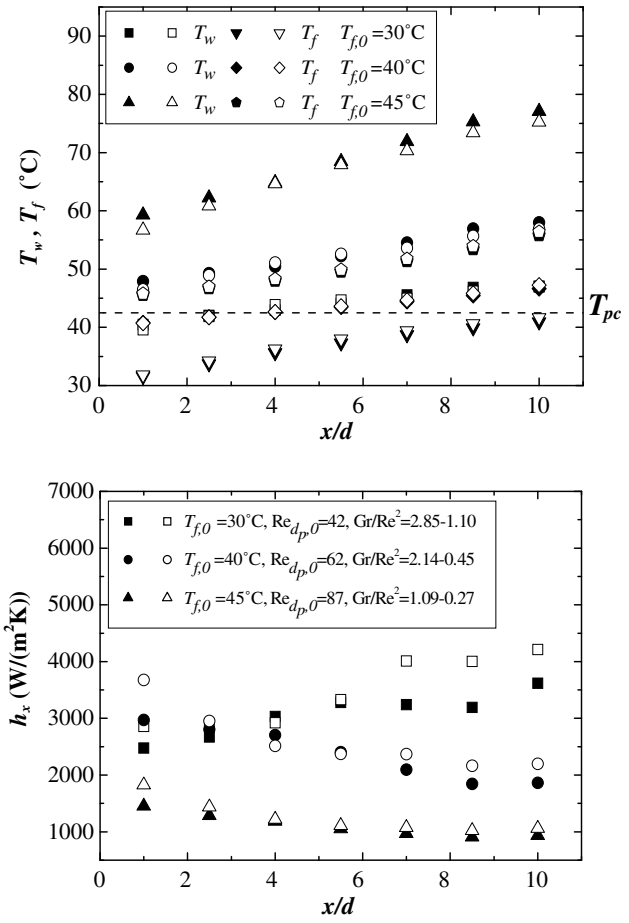

Fig. 4. Local wall and fluid bulk temperatures and local heat transfer coefficients for various inlet temperatures in the porous tube. $d = 4$ mm, $d_p = 0.2$–0.28 mm, $\varepsilon = 0.4$, $p_0 = 9.5$ MPa, $G = 0.5$ kg/h, $q_w = 2.2 \times 10^4$ W/m^2. Solid symbols: upward flow; hollow symbols: downward flow.

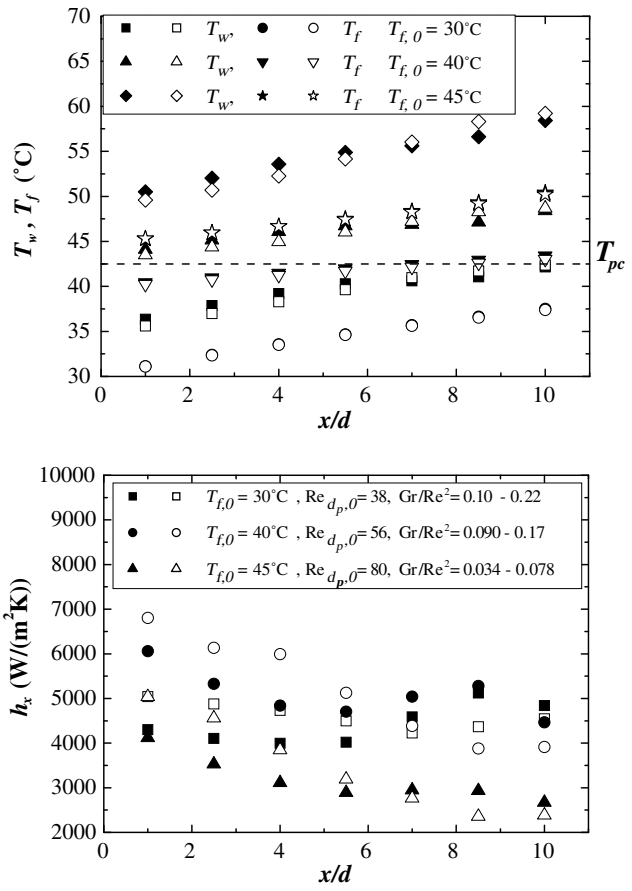

Fig. 5. Local wall and fluid bulk temperatures and local heat transfer coefficients for various inlet temperatures in the porous tube. $d = 4$ mm, $d_p = 0.1$–0.12 mm, $\varepsilon = 0.45$, $p_0 = 9.5$ MPa, $G = 1.0$ kg/h, $q_w = 2.2 \times 10^4$ W/m^2. Solid symbols: upward flow; hollow symbols: downward flow.

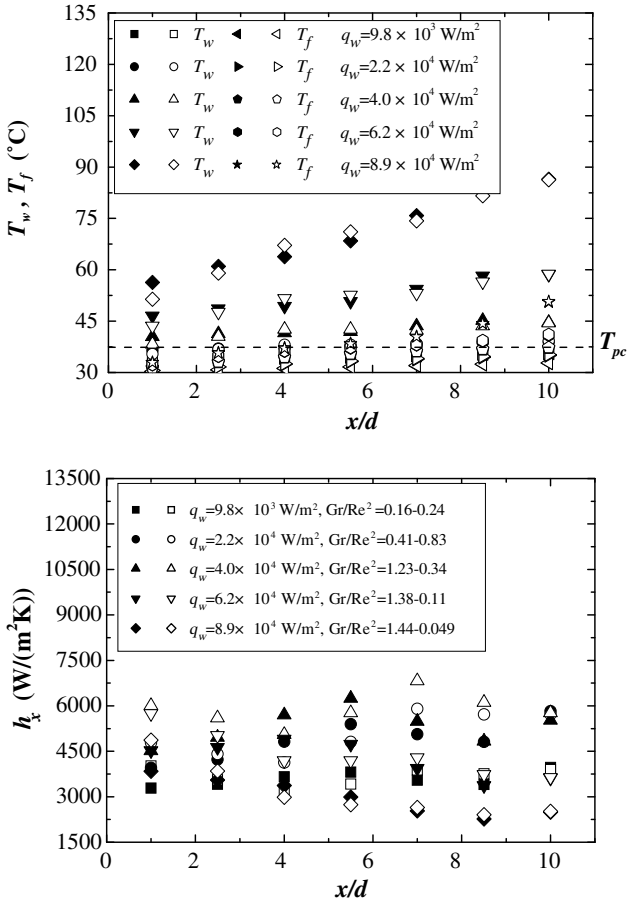

Fig. 6. Local wall and fluid bulk temperatures and local heat transfer coefficients for various heat fluxes in a porous tube. d = 4 mm, d_p = 0.2–0.28 mm, ε = 0.4, p_0 = 8.5 MPa, G = 1.0 kg/h, T_0 = 30 °C, $Re_{d_p,0} = 89$. Solid symbols: upward flow; hollow symbols: downward flow.

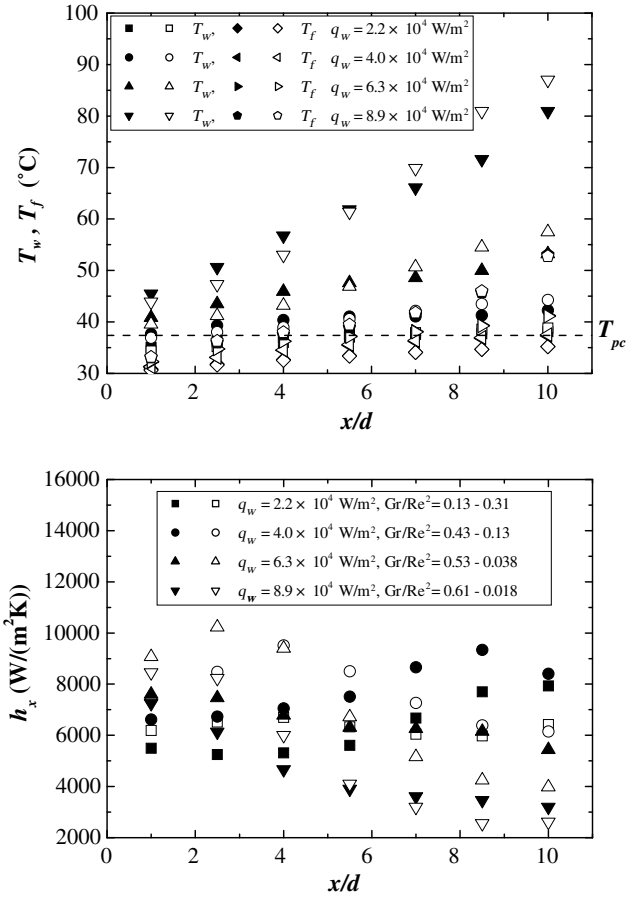

Fig. 7. Local wall and fluid bulk temperatures and local heat transfer coefficients for various heat fluxes in a porous tube. d = 4 mm, d_p = 0.1–0.12 mm, ε = 0.45, p_0 = 8.5 MPa, G = 1.0 kg/h, T_0 = 30 °C, $Re_{d_p,0} = 41$. Solid symbols: upward flow; hollow symbols: downward flow.

flux for both upward and downward flows. This phenomenon is caused by the strong variations of the thermophysical properties, especially the variation of c_p, and depend on the local wall and local fluid temperature relationships. With increasing heat flux, the local CO_2 bulk temperatures and the local wall temperatures increase to above T_{pc}. The very sharp variations of the fluid thermophysical properties include the maximum specific heat which causes the local heat transfer coefficients to reach a maximum with increasing heat flux for $T_0 < T_{pc}$. When the wall temperatures are much larger than T_{pc}, the local heat transfer coefficients decrease uniformly along the porous tube for both upward and downward flows due to the decreases of the thermophysical properties.

The experimental results show that for $T_0 > T_{pc}$, the local heat transfer coefficients decrease with increasing heat flux due to the decreases of the thermophysical properties with increasing temperature (Fig. 3).

The differences of the local heat transfer coefficients along the porous tube for upward and downward flows are mainly caused by buoyancy. However, the influence of buoyancy on the heat transfer along the porous tube is not significant for the studied conditions when compared with empty vertical tubes. The sharp variation of the density with temperature influences the buoyancy in the porous media, creating various fluid and wall temperature distributions. The thermophysical properties of CO_2 at supercritical pressures strongly depend on temperature distributions; therefore, the local heat transfer coefficients along the porous tube for upward and downward flows are somewhat different. The mechanism and quantitative description of the influence of buoyancy should be studied further.

3.3. Influence of mass flow rate

Figs. 8 and 9 show the wall and fluid bulk temperatures and the local heat transfer coefficients for various mass flow rates in the porous tube. Generally, the local heat transfer coefficients increase with increasing mass flow rates. Since the wall temperatures are much larger than T_{pc} for the lower mass flow rate, the thermophysical properties all decrease; therefore, the local heat transfer coefficients decrease continuously along the porous tube for both upward and downward flows. However, for larger mass flow rates, the local heat transfer coefficients change little and have a maximum along the porous tube for both upward and downward flows. The reason is that the specific heat increases and goes through a maximum near T_{pc} when the inlet temperature is lower than T_{pc}.

3.4. Influence of pressure

The effect of pressure on the convection heat transfer in the porous tube is shown in Figs. 10 and 11. The local heat transfer coefficients increase with decreasing pressure (approaching p_c) for both upward and downward flows with the local heat transfer coefficients having maximums when the CO_2 bulk temperatures are near the pseudocritical temperature due to the sharp increase in the specific heat. At the same time, the effect of buoyancy increases with decreasing pressure. However, with the temperature

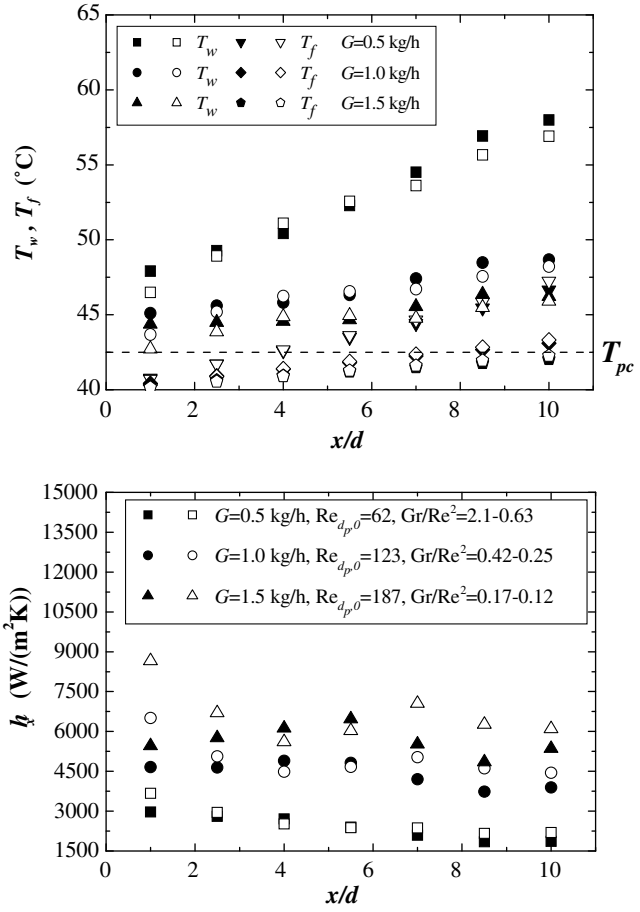

Fig. 8. Local wall and fluid bulk temperatures and local heat transfer coefficients for various mass flow rates in a porous tube. d = 4 mm, d_p = 0.2–0.28 mm, ε = 0.4, p_0 = 9.5 MPa, T_0 = 40 °C, q_w = 2.2 × 10^4 W/m^2. Solid symbols: upward flow, hollow symbols: downward flow.

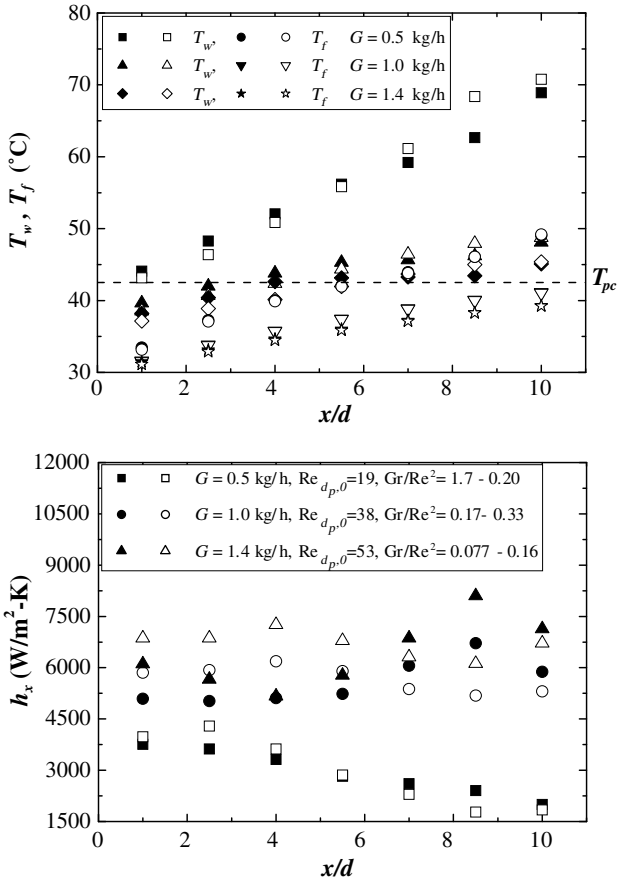

Fig. 9. Local wall and fluid bulk temperatures and local heat transfer coefficients for various mass flow rates in a porous tube. d = 4 mm, d_p = 0.1–0.12 mm, ε = 0.45, p_0 = 9.5 MPa, T_0 = 30 °C, q_w = 4.0 × 10^4 W/m^2. Solid symbols: upward flow, hollow symbols: downward flow.

far from the pseudocritical temperature, the pressure does not have a significant effect on the convection heat transfer.

3.5. Influence of particle diameter

Figs. 12 and 13 show the effect of particle diameter on the convection heat transfer in the two porous tubes. The local heat transfer coefficients in the porous tube with particle diameters 0.1–0.12 mm are larger than those with particle diameters 0.2–0.28 mm for both upward and downward flows for the same conditions. The bronze particle thermal conductivity is much higher than that of CO_2; thus, the thermal conduction through the solid particles and the convection heat transfer between the particles and the CO_2 (the "fin effect") play very important roles in the overall heat transfer from the tube surface. Also, the contact surface area between the particles and the CO_2 increases with decreasing particle diameter, which increases the heat transfer. Therefore, for the conditions studied, the heat transfer coefficients increased with decreasing particle diameter. Again, the reason for the difference between the upward and downward flows should be investigated further.

4. Numerical simulation of the flow and convection heat transfer

4.1. Physical and mathematical models and calculational method

Fig. 14 shows the physical model used in the numerical simulations, which is similar to the experimental test section. The calculational region included the CO_2 flow in the porous media and the tube wall. The flow was considered to be two-dimensional and steady.

The numerical simulations were performed using the computational fluid dynamics program FLUENT 6.2. The FLUENT porous media model was modified to include the effects of variable properties, variable porosity, thermal dispersion and the stagnant effective thermal conductivity by compiling user defined functions.

The governing equations for the local thermal equilibrium model for the porous tube are:

Continuity equation:

$$\frac{1}{r}\frac{\partial}{\partial r}(r\varepsilon v_p) + \frac{\partial}{\partial x}(\varepsilon u_p) = 0 \tag{5}$$

Momentum equations:

$$\frac{\partial}{\partial x}(\rho_f u_p u_p \varepsilon) + \frac{\partial}{\partial r}(\varepsilon \rho_f u_p v_p) = -\frac{\partial}{\partial x}(\varepsilon p) + \varepsilon\mu_f\left[\frac{\partial^2 u_p}{\partial x^2} + \frac{1}{r}\frac{\partial}{\partial r}\left(r\frac{\partial u_p}{\partial r}\right)\right] - \frac{\varepsilon\mu_f u_p}{K} - \frac{\varepsilon^3\rho_f F}{K^{1/2}}|\vec{V}_p|u_p - \rho g\varepsilon \tag{6}$$

$$\frac{\partial}{\partial x}(\rho_f u_p v_p \varepsilon) + \frac{\partial}{\partial r}(\varepsilon \rho_f v_p v_p) = -\frac{\partial}{\partial r}(\varepsilon p) + \varepsilon\mu_f\left[\frac{\partial^2 v_p}{\partial x^2} + \frac{1}{r}\frac{\partial}{\partial r}\left(r\frac{\partial v_p}{\partial r}\right)\right] - \frac{\varepsilon\mu_f v_p}{K} - \frac{\varepsilon^3\rho_f F}{K^{1/2}}|\vec{V}_p|v_p \tag{7}$$

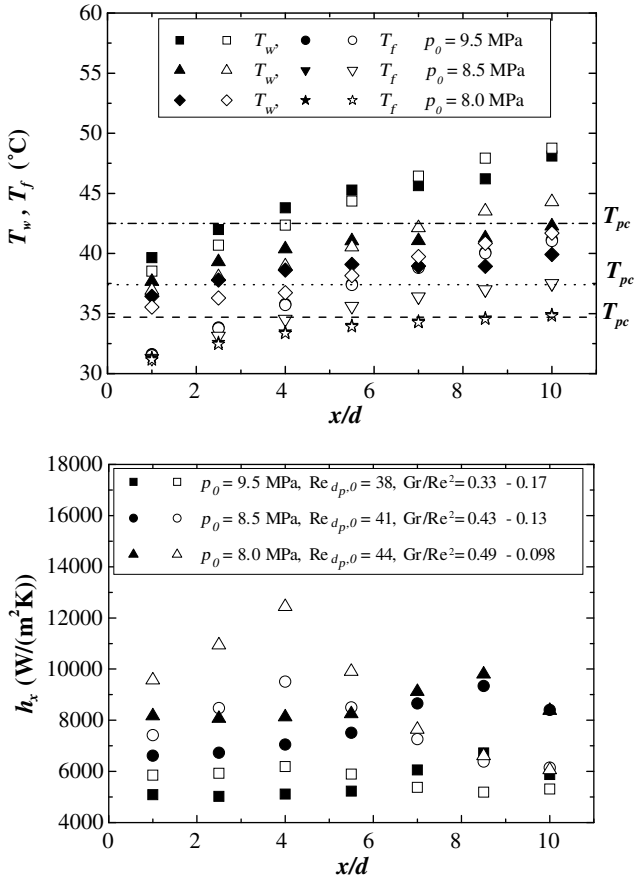

Fig. 10. Local wall and fluid bulk temperatures and local heat transfer coefficients for various pressures in a porous tube. d = 4 mm, d_p = 0.1–0.12 mm, ε = 0.45, G = 1.0 kg/h, $q_w = 4.0 \times 10^4$ W/m², T_0 = 30 °C. Solid symbols: upward flow, hollow symbols: downward flow.

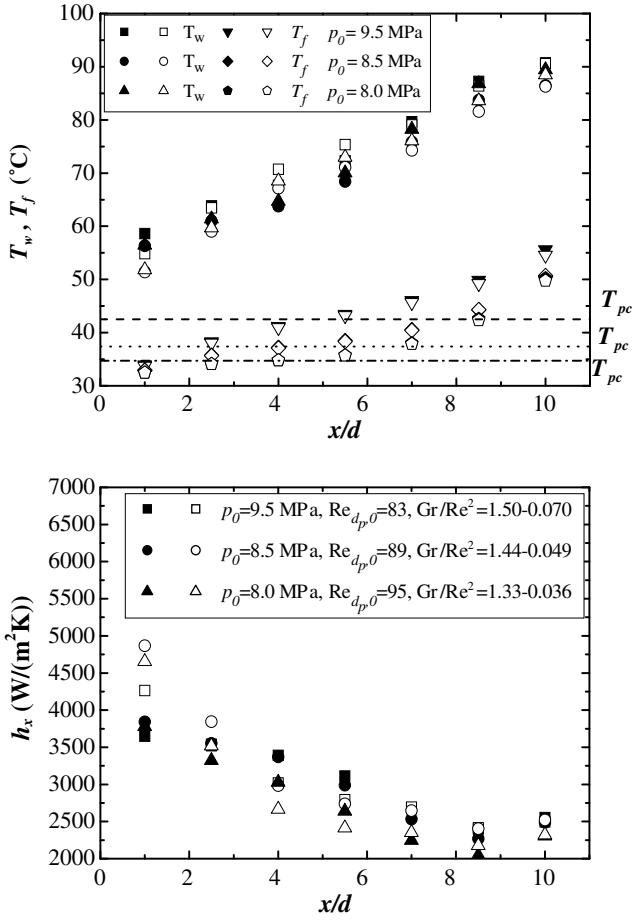

Fig. 11. Local wall and fluid bulk temperatures and local heat transfer coefficients for various pressures in a porous tube. d = 4 mm, d_p = 0.2–0.28 mm, ε = 0.4, G = 1.0 kg/h, $q_w = 8.9 \times 10^4$ W/m², T_0 = 30 °C. Solid symbols: upward flow, hollow symbols: downward flow.

Energy equation:

$$\frac{\partial}{\partial x}(\varepsilon\rho_f u_p h_f) + \frac{\partial}{\partial r}(\varepsilon\rho_f v_p h_f) = \frac{1}{r}\frac{\partial}{\partial r}\left[rk_{eff}\frac{\partial T}{\partial r}\right] + \frac{\partial}{\partial x}\left(k_{eff}\frac{\partial T}{\partial x}\right) \tag{8}$$

The parameters used in these equations were taken from Vafai and Amiri [29] and Hsu et al. [30] and Cheng et al. [31]:

$$K = \frac{d_p^2}{a}\frac{\varepsilon^3}{(1-\varepsilon)^2}, \quad F = \frac{b}{\sqrt{a}\varepsilon^{3/2}}, \quad a = 215, \quad b = 1.92 \tag{9}$$

$$k_{eff} = k_{sta} + k_{dis} \tag{10}$$

$$\frac{k_{sta}}{k_f} = \left[1-\sqrt{1-\varepsilon}\right] + \frac{\sqrt{1-\varepsilon}}{\sigma}\left[1-\frac{1}{(1+\alpha B)^2}\right] + \frac{2\sqrt{1-\varepsilon}}{[1-\sigma B+(1-\sigma)\alpha B]} \times \left[\frac{(1-\sigma)(1+\alpha)B}{[1-\sigma B+(1-\sigma)\alpha B]^2}\ln\left(\frac{1+\alpha B}{(1+\alpha)\sigma B}\right) - \frac{B+1+2\alpha B}{2(1+\alpha B)^2} - \frac{B-1}{[1-\sigma B+(1-\sigma)\alpha B](1+\alpha B)}\right] \tag{11}$$

$\sigma = k_f/k_s$, $\alpha = 0.002$ for $\varepsilon_m = 0.4$ and $\alpha = 0.025$ for $\varepsilon_m = 0.45$

B was calculated from

$$\varepsilon = 1 - \frac{B^2}{(1-B)^6(1+\alpha B)^2}\left[(B^2-4B+3)+2(1+\alpha)(1+\alpha B) \times \ln\frac{(1+\alpha)B}{1+\alpha B} + \alpha(B-1)(B^2-2B-1)\right]^2 \tag{12}$$

$$k_{dis} = C(1-\varepsilon)(\rho c_p)_f\sqrt{u_p^2+v_p^2}d_p, \quad C = 0.04 \tag{13}$$

$$\varepsilon = \varepsilon_\infty[1 + C_1\exp(-N_1(r_o-r)/d_p)], \quad C_1 = \frac{\varepsilon_w}{\varepsilon_\infty} - 1, \quad N_1 = 6,$$

$\varepsilon_w = 0.8$, for a cylindrical tube

$$\varepsilon_\infty = \frac{\varepsilon_m}{1+\frac{2C_1 d_p}{N_1 r_o^2}\left\{r_o - \frac{d_p}{N_1}[1-\exp(-N_1 r_o/d_p)]\right\}} \tag{14}$$

The boundary conditions were selected according to the experimental conditions. The velocity inlet and pressure outlet boundary conditions were used in the simulations. The outside wall of the porous part of the calculational zone had a constant heat flux with all the other walls were insulated. The temperature distributions in the solid wall and the porous fluid zone were solved simultaneously.

The NIST Standard Reference Database 23 (REFPROP) Version 7.1 was used to calculate the temperature and pressure dependent properties of carbon dioxide. The SIMPLEC algorithm was used to couple the pressure and velocities. The second order upwind scheme was used in the momentum, energy, turbulent kinetic

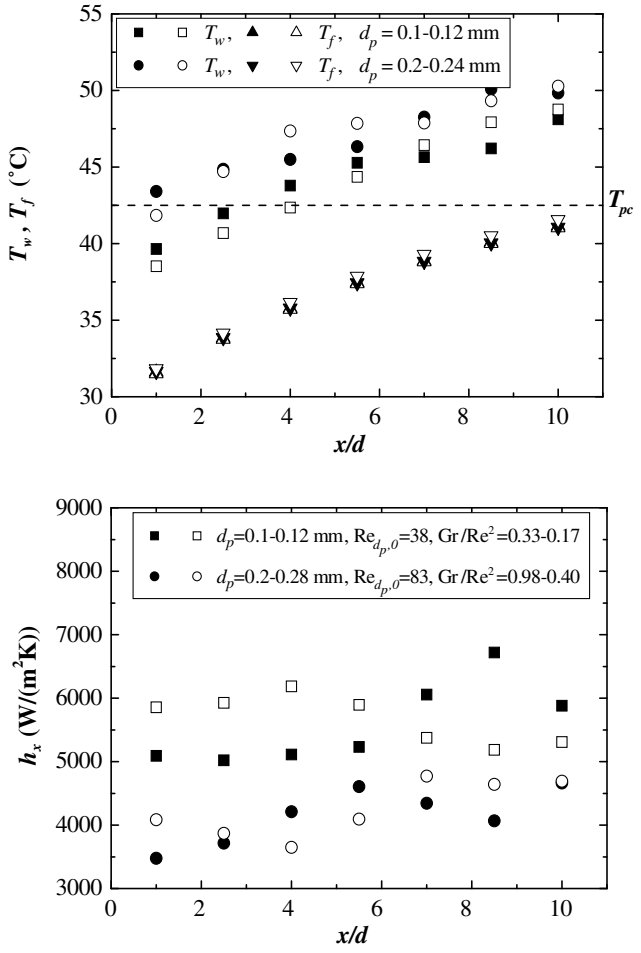

Fig. 12. Local wall and fluid bulk temperatures and local heat transfer coefficients for various particle diameters. d = 4 mm, p = 9.5 MPa, q_w= 4.0×10^4 W/m^2, G = 1.0 kg/h, T_0 = 30 °C. Solid symbols: upward flow, hollow symbols: downward flow.

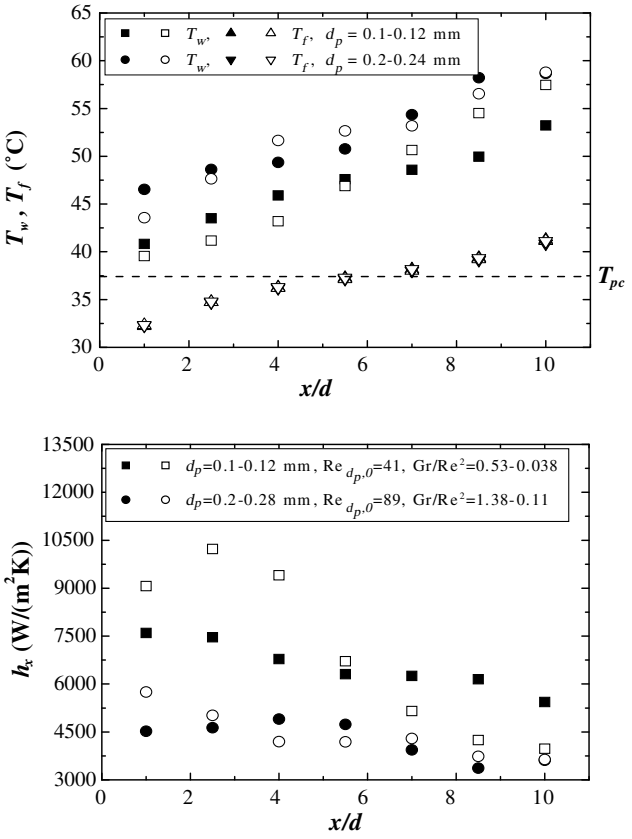

Fig. 13. Comparison of local wall and fluid bulk temperatures and local heat transfer coefficients for various particle diameters d = 4 mm, p = 8.5 MPa, q_w = 6.3×10^4 W/m^2, G = 1.0 kg/h, T_0 = 30 °C. Solid symbols: upward flow, hollow symbols: downward flow.

energy, and turbulent energy dissipation equations. The convergence criteria required a decrease of at least five orders of magnitude for the residuals with no observable change in the outlet temperatures for an additional 200 iterations. Calculations with various numbers of elements in the axial direction and in the radial direction showed that the results with 400 nodes in the axial direction and (150 + 30) nodes in the radial direction (fluid region + tube wall) were grid independent. The standard k–ε turbulence model with enhanced wall function was used to calculate the flows in the inlet and outlet regions where there was no porous media.

4.2. Numerical results for the friction factor in the porous tube

Previous works [24,27] showed that the friction factor, f_e, calculated from the experimental data for normal fluids such as water and air in porous media with enough particles in the test section cross-section can be well predicted using [32]:

$$f_e = \frac{\varepsilon_m^3}{1-\varepsilon_m}\frac{\rho_f d_p}{3M^2}\frac{\Delta p}{L} = \frac{36.4}{Re_e} + 0.45 \quad (\text{for } Re_e < 2000) \tag{15}$$

where Re_e is the equivalent Reynolds number defined as: $Re_e = \frac{2Md_p}{3\mu_f(1-\varepsilon)}$.

Jiang et al. [14] showed that the friction factor of CO_2 at supercritical pressures at a constant temperature (without heating) in the sintered porous tube with particle diameters of 0.2–0.28 mm corresponded very well with Eq. (15).

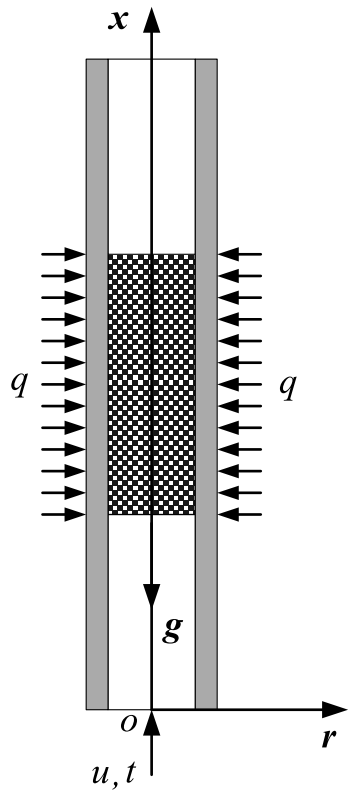

Fig. 14. Physical model and coordinate system for numerical simulation.

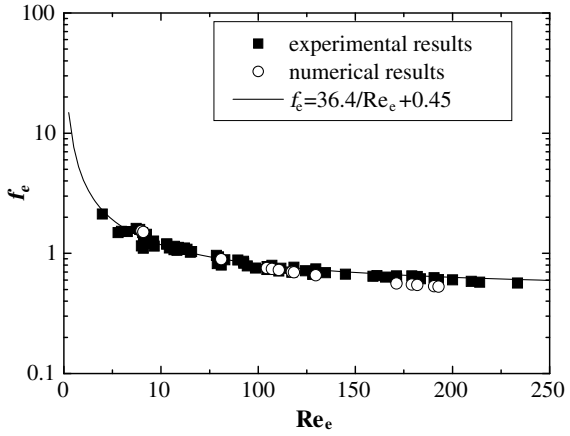

Fig. 15. Friction factor for CO_2 at supercritical pressures in sintered porous tubes without heating: p = 7.7–9.7 MPa, $T_{f,b}$ = 23 – 29 °C, G = 0.5–2.4 kg/h, d_p = 0.1–0.12 mm and 0.2–0.28 mm.

Fig. 15 compares the friction factor, f_e, predicted by the numerical simulations with the experimental data for CO_2 at supercritical pressures with a constant temperature (without heating) in the sintered porous tube and f_e predicted by Eq. (15). The numerically calculated values of f_e correspond well to the experimental data and the values predicted using Eq. (15).

However, for the heated sintered porous tube, the numerically calculated values of f_e differ greatly from the experimental data. The difference may be attributed to the assumption of thermal equilibrium used in the numerical simulation which differs from the experimental conditions, and the sharp variations of the thermophysical properties with temperature which may significantly influence the flow characteristics. The effect of buoyancy on the convection heat transfer caused by the strong variation of the thermophysical properties of supercritical pressure CO_2 cannot be well predicted by the thermal equilibrium model. Therefore, a thermal non-equilibrium model should be developed for numerical simulations of fluid flow of CO_2 at supercritical pressures.

4.3. Numerical results for convection heat transfer in porous tubes

Fig. 16 compares the measured and predicted wall temperatures for supercritical pressure CO_2 flowing in a vertical heated sintered porous tube with d_p = 0.2–0.28 mm when the inlet temperatures are lower but close to the pseudocritical temperature. The data shows that the local thermal equilibrium model considering variable thermophysical properties, variable porosity, thermal dispersion and area-of-contact stagnant effective thermal conductivity accurately predict the measured wall temperatures when the wall temperature was much higher than T_{pc}. In addition, for the studied conditions the influence of buoyancy on the convection heat transfer is not significant.

The velocity distributions across the tube for various heat fluxes in Fig. 17a show that the velocity increases with increasing heat flux, and the velocity has a peak close to the heated wall due to the decrease in the density. As shown in Fig. 16, the wall temperature at x/d = 7 increases with increasing heat flux on the wall and is much higher than T_{pc} for heat fluxes of 6.2×10^4 W/m^2 and 8.9×10^4 W/m^2. Fig. 3 shows that the density decreases sharply with increasing temperature. Therefore, the velocity of CO_2 close to the heated wall increases sharply to a maximum and then

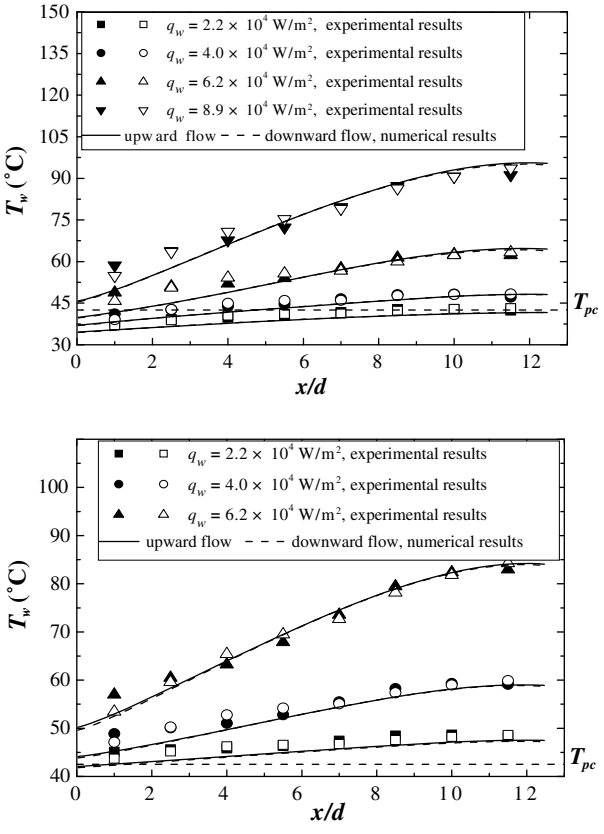

Fig. 16. Comparison of the measured and calculated wall temperatures. d = 4 mm, d_p = 0.2–0.28 mm, ε = 0.4, p = 9.5 MPa, G = 1.0 kg/h: (a) T_0 = 30 °C and (b) T_0 = 40 °C. Solid symbols: upward flow, hollow symbols: downward flow.

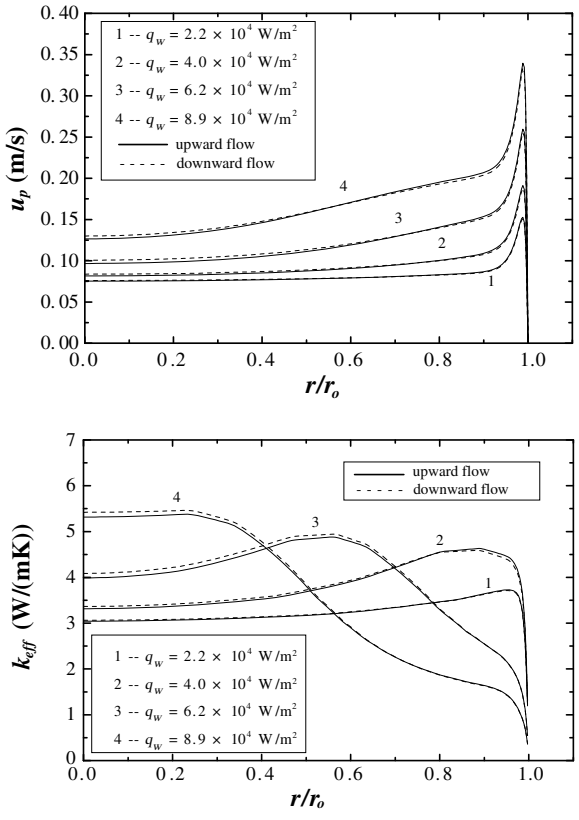

Fig. 17. Property distributions in the cross-section at x/d = 7: (a) velocity and (b) effective thermal conductivity. d = 4 mm, d_p = 0.2–0.28 mm, ε = 0.4, p = 9.5 MPa, G = 1.0 kg/h, T_0 = 30 °C.

decreases towards the tube center when the temperature is lower and the density is relatively higher.

The effective thermal conductivity of the porous media, k_{eff}, varies significantly with heat flux and across the tube section as shown in Fig. 17b. The k_{eff} near the heated wall first increases and then decreases with increasing heat flux. Eqs. (10)–(13) show that the effective thermal conductivity of the porous media increases with increasing $\rho_f c_{pf} u_p$. The complex variations of k_{eff} in the porous tube are caused by the sharp variations of density, specific heat and velocity in the tube. The variation of the effective thermal conductivity with increasing heat flux may be the reason for the convection heat transfer first increasing to a maximum and then decreasing with increasing heat flux as discussed in Section 3.2.

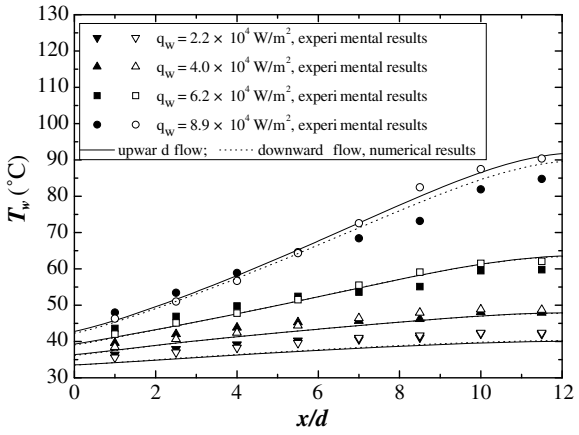

Fig. 18. Comparison of measured and calculated wall temperatures. $d = 4$ mm, $d_p = 0.1$–0.12 mm, $\varepsilon = 0.45$, $p = 9.5$ MPa, $G = 1.0$ kg/h, $T_0 = 30$ °C. Solid symbols: upward flow, hollow symbols: downward flow.

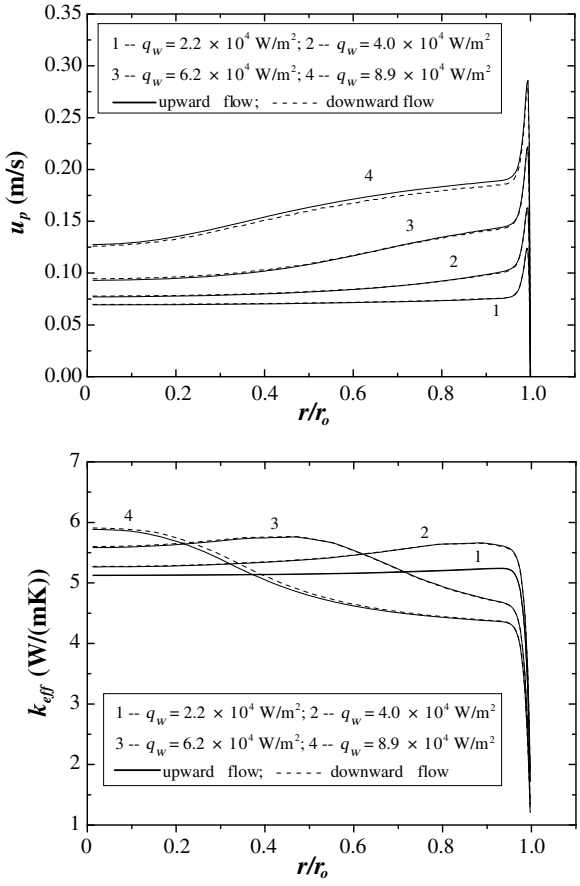

Fig. 19. Property distributions in the cross-section at $x/d = 7$: (a) velocity and (b) effective thermal conductivity. $d = 4$ mm, $d_p = 0.1$–0.12 mm, $\varepsilon = 0.45$, $p = 9.5$ MPa, $G = 1.0$ kg/h, $T_0 = 30$ °C.

Fig. 18 compares the measured and the predicted wall temperatures for supercritical pressure CO_2 flowing in a vertical heated sintered porous tube with $d_p = 0.1$–0.12 mm when the inlet temperatures are lower than the pseudocritical temperature. The numerical results with the local thermal equilibrium model considering variable thermophysical properties, variable porosity, thermal dispersion and area-of-contact stagnant effective thermal conductivity correspond well to the measured wall temperatures using the deformation factor $\alpha = 0.025$ in the correlation for the stagnation thermal conductivity, Eq. (11). The velocity distributions and the effective thermal conductivity for the different heat fluxes are shown in Fig. 19 follow the same variations as those for $d_p = 0.2$–0.28 mm in Fig. 17.

Figs. 17b and 19b show that the effective thermal conductivities in the porous tube with particle diameters 0.1–0.12 mm are larger than those with particle diameters 0.2–0.28 mm. This is one of the reasons for the higher local heat transfer coefficients in the porous tube with particle diameters 0.1–0.12 mm than in the tube with particle diameters 0.2–0.28 mm for both upward and downward flows for the same conditions as discussed in Section 3.5.

5. Conclusions

When the wall temperatures are much larger than T_{pc}, the local heat transfer coefficients decrease uniformly along the porous tube for both upward and downward flows. However, for $T_0 < T_{pc}$ and wall temperatures slightly higher than T_{pc}, the local heat transfer coefficients have a maximum for both upward and downward flows along the porous tube when the fluid bulk temperatures are near T_{pc}.

Buoyancy influences the convection heat transfer in the porous media causing different variations of the local heat transfer coefficients along the porous tube for upward and downward flows.

The numerically calculated values of f_e correspond well to the experimental data and the values predicted using the friction factor correlation without heating. However, the predicted friction factors in the heated sintered porous tube differ from the experimental results.

The convection heat transfer of supercritical pressure CO_2 in porous media can be properly predicted by the local thermal equilibrium model when the wall temperature is much higher than T_{pc}. The effective thermal conductivity plays an important role on the convection heat transfer of supercritical pressure CO_2 in porous media.

The velocity increases with increasing heat flux with a peak close to the heated wall due to the decrease of the density.

The effective thermal conductivity of the porous media significantly varies with heat flux and across the tube section. The effective thermal conductivities in the porous tube with particle diameters 0.1–0.12 mm are larger than those with particle diameters 0.2–0.28 mm.

Acknowledgements

The project was supported by the Key Project Fund from the National Natural Science Foundation of China (No. 50736003) and by the Tsinghua Basic Research Foundation (No. JCpy2005049). We thank Professor J.D. Jackson in the School of Mechanical, Aerospace and Civil Engineering, the University of Manchester, UK, for many

discussions and good suggestions for the research. We also thank Prof. David Christopher for editing the English.

References

[1] B.S. Petukhov, Heat transfer and friction in turbulent pipe flow with variable physical properties, Adv. Heat Transfer 6 (1970) 503–564.
[2] W.B. Hall, Heat transfer near the critical point, Adv. Heat Transfer 7 (1971) 1–86.
[3] J.D. Jackson, Some striking features of heat transfer with fluids at pressures and temperatures near the critical point, in: Proceedings of the International Conference on Energy Conversion and Application (ICECA '2001), vol. 1, 2001, pp. 50–61.
[4] E.A. Krasnoshchekov, V.S. Protopopov, Experimental study of heat exchange in carbon dioxide in the supercritical range at high temperature drops (in Russian), Teplofizika Vysokikh Temperatur 4 (1966) 389–398.
[5] V.S. Protopopov, Generalized correlations for local heat transfer coefficient for turbulent flow of water and carbon dioxide at super-critical pressure in uniformed heated tubes (in Russian), Teplofizika Vysokikh Temperatur 15 (1977) 815–821.
[6] V.N. Popov, Ye.P. Valueva, Mixed turbulent fluid convection in vertical tubes (in Russian), Teploenergetika 2 (1988) 17–22.
[7] V.A. Kurganov, A.G. Kaptilnyi, Flow structure and turbulent transport of a supercritical pressure fluid in a vertical heated tube under the conditions of mixed convection: experimental data, Int. J. Heat Mass Transfer 36 (1993) 3383–3392.
[8] P.X. Jiang, Z.P. Ren, B.X. Wang, Convective heat and mass transfer of water at supercritical pressures under heating or cooling conditions in vertical tubes, J. Therm. Sci. 4 (1995) 15–25.
[9] S. He, W.S. Kim, P.X. Jiang, J.D. Jackson, Simulation of mixed convection heat transfer to carbon dioxide at supercritical pressure, J. Mech. Eng. Sci. 218 (2004) 1281–1296.
[10] S.M. Liao, T.S. Zhao, An experimental investigation of convection heat transfer to supercritical carbon dioxide in miniature tubes, Int. J. Heat Mass Transfer 45 (2002) 5025–5034.
[11] P.X. Jiang, Y.J. Xu, J. Lv, R.F. Shi, S. He, J.D. Jackson, Experimental investigation of convection heat transfer of CO_2 at supercritical pressures in vertical mini tubes and in porous media, Appl. Therm. Eng. 24 (2004) 1255–1270.
[12] S. He, P.X. Jiang, Y.J. Xu, R.F. Shi, W.S. Kim, J.D. Jackson, A computational study of convection heat transfer to CO_2 at supercritical pressures in a vertical mini tube, Int. J. Therm. Sci. 44 (2005) 521–530.
[13] P.X. Jiang, B.X. Wang, D.A. Luo, Z.P. Ren, Fluid flow and convective heat transfer in a vertical porous annulus, Numer. Heat Transfer: Part A 30 (1996) 305–320.
[14] P.X. Jiang, R.F. Shi, Y.J. Xu, S. He, J.D. Jackson, Experimental investigation of flow resistance and convection heat transfer of CO_2 at supercritical pressures in a vertical porous tube, J. Supercrit. Fluids 38 (2006) 339–346.
[15] K. Vafai, C.L. Tien, Boundary and inertial effects on flow and heat transfer in porous media, Int. J. Heat Mass Transfer 24 (1981) 195–203.
[16] P. Cheng, C.T. Hsu, Fully-developed forced convective flow through an annular packed-sphere bed with wall effects, Int. J. Heat Mass Transfer 29 (1986) 1843–1853.
[17] M.L. Hunt, C.L. Tien, Non-Darcy convection in cylindrical packed beds, J. Heat Transfer 110 (1988) 378–384.
[18] C.T. Hsu, P. Cheng, Thermal dispersion in a porous medium, Int. J. Heat Mass Transfer 33 (1990) 1587–1597.
[19] A. Amiri, K. Vafai, T.M. Kuzay, Effects of boundary conditions on non-Darcian heat transfer through porous media and experimental comparisons, Numer. Heat Transfer: Part A 27 (1995) 651–664.
[20] U.A. Jeigarnik, F.P. Ivanov, N.P. Ikranikov, Experimental data on heat transfer and hydraulic resistance in unregulated porous structures (in Russian), Teploenergetika 2 (1991) 33–38.
[21] E. Achenbach, Heat and flow characteristics of packed beds, Exp. Therm. Fluid Sci. 10 (1995) 17–27.
[22] J.L. Lage, A.K. Weinert, D.C. Price, R.M. Weber, Numerical study of a low permeability microporous heat sink for cooling phased-array radar systems, Int. J. Heat Mass Transfer 39 (1996) 3633–3647.
[23] M. Quintard, Modelling local non-equilibrium heat transfer in porous media, in: J.S. Lee (Ed.), Proceedings of 11th International Heat Transfer Conference, vol. 1, 1998, pp. 279–285.
[24] P.X. Jiang, Z. Wang, Z.P. Ren, B.X. Wang, Experimental research of fluid flow and convection heat transfer in porous plate channels filled with glass or metallic particles, Exp. Therm. Fluid Sci. 20 (1999) 45–54.
[25] P.X. Jiang, Z.P. Ren, Numerical investigation of forced convection heat transfer in porous media using a thermal non-equilibrium model, Int. J. Heat Fluid Flow 22 (2001) 102–110.
[26] B. Alazmi, K. Vafai, Constant wall heat flux boundary conditions in porous media under local thermal non-equilibrium conditions, Int. J. Heat Mass Transfer 45 (2002) 3071–3087.
[27] P.X. Jiang, M. Li, T.J. Lu, L. Yu, Z.P. Ren, Experimental research on convection heat transfer in sintered porous plate channels, Int. J. Heat Mass Transfer 47 (2004) 2085–2096.
[28] E.W. Lemmon, M.O. McLinden, M.L. Huber, Reference Fluid Thermodynamic and Transport Properties, NIST Standard Reference Database 23, Version 7.1, 2003.
[29] K. Vafai, A. Amiri, Non-Darcian effects in confined forced convective flows, in: D.B. Ingham, I. Pop (Eds.), Transport Phenomena in Porous Media, Pergamon, Oxford, 1998, pp. 313–329.
[30] C.T. Hsu, P. Cheng, K.W. Wong, Modified Zehner–Schlunder models for stagnant thermal conductivity of porous media, Int. J. Heat Mass Transfer 37 (17) (1994) 2751–2759.
[31] P. Cheng, A. Chowdhury, C.T. Hsu, Forced convection in packed tubes and channels with variable porosity and thermal dispersion effects, in: S. Kakac, B. Kilkis, F.A. Kulacki, et al. (Eds.), Convective Heat and Mass Transfer in Porous Media, Kluwer Academic Publishers, 1991, pp. 625–653.
[32] M.E. Aerov, O.M. Tojec, Hydraulic and Thermal Basis on the Performance of Apparatus with Stationary and Boiling Granular Layer (in Russian), Himia Press, Leningrad, 1968.